Pass-through photon-based biomedical transillumination

Paulino Vacas-Jacques
Gonzalo Paez
Marija Strojnik
Centro de Investigaciones en Optica
Apartado Postal 1-948
37000, Leon, Guanajuato
Mexico

Abstract. We present the mathematical foundation and the experimental validation of a technique that utilizes pass-through (ballistic) photons in a partial coherence interferometric transillumination setup for biomedical analyses. We demonstrate that the implementation depends closely on tissue under test, incident power, spatial and spectral characteristics of the radiation source, and detection electronics. With the aid of the complex material coherence function concept, we foresee tissue characterization and diagnostic imaging as potential applications for the technique. We propose a normalization procedure for *in vitro* and *in vivo* measurements, where nontissue-related quantities are canceled out. The validation of the proposal is achieved by obtaining the sample coherence function of a tissue phantom. The expected exponential attenuation is confirmed, and the corresponding scattering coefficients are determined. A good agreement between theory and experiment, for the initial set of samples, serves to establish that pass-through photon-based transillumination is feasible for selected biomedical applications. [DOI: 10.1117/1.2953191]

Keywords: transillumination; partial coherence interferometry; calibration; tissue characterization; tissue imaging; tissue phantom.

Paper 07313SSRR received Aug. 6, 2007; revised manuscript received Feb. 23, 2008; accepted for publication Feb. 26, 2008; published online Aug. 11, 2008.

1 Introduction

One of the key aspects in biomedical diagnosis is the characterization of tissue samples. Several different approaches may be utilized to describe tissue, depending on the specific properties of the sample under study. Moreover, the expected outcome from such an assessment needs also be taken into account to decide which method is most suitable for characterizing the sample. In addition, cost constraints play an important role while implementing a chosen diagnostic technique. For instance, a recent study suggests that acoustic densitometry may represent a useful tool for the evaluation of myocardial tissue changes in patients with chronic kidney disease.[1] Meanwhile, an optical technique has also been utilized, for a different application, to characterize myocardial tissue.[2] Thus different considerations must be evaluated before a choice is made for a specific tissue characterization technique.

Many current techniques in optical-biomedical diagnosis emphasize the importance of using backscattered or reflected radiation as a principal source of information.[3–12] In radiation-tissue interactions, however, several other phenomena take place in addition to backscattering and reflection. Most important for our application is transillumination of scattered (i.e., diffuse) and pass-through (i.e., ballistic) photons.[13] We are interested in providing a diagnostic technique that utilizes pass-through photons as a principal source of information to achieve two goals. On the one hand, we would like to characterize tissue via the complex material coherence function describing the sample.[14] On the other hand, we desire to perform diagnostic imaging.[15,16] The challenges associated with the technique are attributed to the low transmission of unscattered photons through tissue. This is indeed the case, because the amount of transmitted ballistic photons is one percent, or less, of the scattered ones. To minimize this impediment, we have proposed a calibration method to isolate the pass-through radiation from the forward-scattered one.[17,18]

During the past two decades, other transillumination modalities relying on time-resolved, frequency-domain, or coherent detection methods have been investigated for biomedical applications. Time-resolved transillumination techniques irradiate the tissue under test with a pulsed light source.[19–22] The applications of time-resolved transillumination are numerous. For instance, an indirect transillumination approach was developed based on optical coherence tomography.[23] This method used a femtosecond pulsed laser as radiation source and a time-gating technique for photon retrieval. Furthermore, with this technique, thick tissue samples were examined with the use of early arriving diffuse light.[24] Another area of knowledge that has greatly benefited from pico- or femtosecond pulse transillumination is optical mammography.[25] In this field, time-correlated single photon counting has been used to image breast and to detect lesions in these tissues.[26,27] Other approaches for generating the discriminating gate for transillumination diagnosis include the utilization of either the degree of optical polarization or coherence.[28–32] Optical imaging through filamentous tissues is one intended application of such diagnostic techniques.[33]

Address all correspondence to: Paulino Vacas-Jacques, Centro de Investigaciones en Optica, Apartado Postal 1-948, 37000, Leon, Guanajuato, Mexico. Tel: 52 477 4414200: Fax: 52 477 4414209; E-mail: pvj@cio.mx

1083-3668/2008/13(4)/041307/10/$25.00 © 2008 SPIE

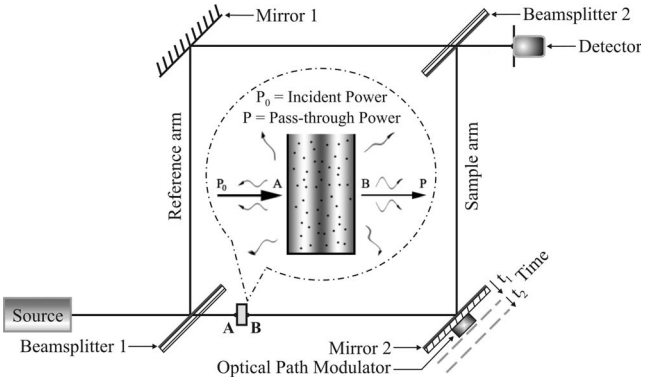

Fig. 1 Time-domain transillumination interferometer proposed for characterizing tissue and performing diagnostic imaging.

In frequency-domain photon migration methods, the formation of photon density waves arises due to the interaction of intensity-modulated light propagating through turbid media (or tissue). The dispersion of these density waves depends on the defining properties of the tissue, and thus serves to characterize the sample under study.[34,35] Furthermore, the detailed description of the properties of photon density waves has been well studied.[36,37] These density waves (i.e., frequency-domain methods) have also been used in transillumination experiments. For example, the clinical importance of breast cancer detection (and treatment) has prompted researchers to investigate the use of frequency-domain techniques to enhance optical mammography.[38] In this same research direction, a transillumination technique implementing the most probable diffuse path calculations for locating inhomogeneities in tissue has been proposed.[39] More recently, a low-coherence setup has been suggested for improving sampling rates for hemodynamic imaging.[40]

Biomedical diagnostic techniques such as optical coherence tomography/microscopy (OCT/OCM) and coherent detection imaging (CDI) benefit from coherent detection methods. Two major differences may be pointed out while considering OCT/OCM and CDI. First, OCT and OCM utilize short coherence radiation sources. Meanwhile, CDI uses long coherence sources to perform diagnosis. Second, the former methods are utilized mostly in a reflection-based geometry, whereas the latter uses a transillumination setup. Coherent detection methods for transillumination analysis were proposed more than a decade ago.[41,42] In this approach, two optical waves of different frequencies are mixed at a photosensitive device, such as a square-law detector. Its implementation for coherent detection imaging has been described in detail.[43,44] Examples of the application of CDI in biomedical transillumination include polarization gating methods for imaging through turbid media,[45] measurement of Wigner phase-space distributions for biomedical applications,[46] and transillumination computed tomography for biomedical sensing.[47,48]

As mentioned before, diverse methods may be utilized for pass-through photon-based transillumination diagnosis. In our approach, we have suggested a time-domain interferometric system, shown schematically in Fig. 1. Ultrafast radiation sources have not been employed. These sources are still rather bulky and expensive, which restricts their implementation. In addition, time-domain interferometry is a well-established technique. This feature helps lessen the instrumentation costs. In contrast, some frequency-domain techniques employ several radiation sources, in conjunction with an electronic oscillator, to produce photon density waves. Furthermore, certain frequency-domain implementations incorporate more expensive instrumentation, for instance, spectrometers. Similarly, coherent detection methods require frequency modulators to generate signal and oscillator beams. In biomedical optics, such beams are frequently produced by acousto-optic modulators, which in turn represent costly instrumentation.

We present a mathematical model describing the time-domain interferometric system, where ballistic radiation is employed for diagnosis. Furthermore, our experimental results demonstrate the feasibility of implementing a pass-through photon-based transillumination system for selected biomedical applications.

2 Theory

The reference and sample electrical fields arriving at the detection plane (refer to Fig. 1) are described by the following equations.[13,17]

$$E_r(\vec{\mathbf{r}}) = E_r \exp\left\{-i\frac{2\pi}{\lambda}\left[\Delta\varphi_0 + 2n_{\text{air}}d + n_{\text{air}}\sum_i D_i(\vec{\mathbf{r}})\right]\right\} \quad \left[\frac{\text{V}}{\text{m}}\right], \tag{1}$$

$$E_s(\vec{\mathbf{r}},t) = E_s\left[\mathcal{R}_g \exp\left(-\frac{1}{2}\sum_i \{[\mu_{a_i}(\vec{\mathbf{r}}) + \mu_{s_i}(\vec{\mathbf{r}})]D_i(\vec{\mathbf{r}})\}\right)\right] \times \exp\left[-i\frac{2\pi}{\lambda}\left(2n_g d + \sum_i [n_{s_i}(\vec{\mathbf{r}})D_i(\vec{\mathbf{r}})] + vtn_{\text{air}}\right)\right] \left[\frac{\text{V}}{\text{m}}\right]. \tag{2}$$

Here subscripts r and s denote reference and sample arms, respectively. E_r and E_s stand for the real amplitude of the electrical fields. λ is wavelength. $\Delta\varphi_0$ represents the path difference between interferometer arms, caused, for example, by mirror and beamsplitter coatings. The thickness of the container wall (for *in vitro* studies) is denoted by d. We designate the sample thickness of the i'th constituent on a layered-like sample as $D_i(\vec{\mathbf{r}})$, where the vector $\vec{\mathbf{r}}$ represents a point of probe. n_{air}, n_g, and n_{si} are the refractive indices of air, container glass, and the i'th sample in that order. The Fresnel reflection coefficient $\mathcal{R}_g$ is also considered. μ_{ai} and μ_{si} correspond to the i'th absorption and scattering coefficient of the sample, whereas the path-length modulation velocity and time delay are represented by v and t correspondingly.

In Eq. (1), we assume that no path-length compensation is necessary and thus the index of refraction of air. The expressions are slightly modified if a compensator is used. The relation in Eq. (2) can be further simplified by introducing the concept of the (complex) material coherence function (MCF).[14] The MCF contains information about the characteristics of the sample to decrease the degree of coherence of a coherent beam on its passing through it. Taking this concept into account, Eq. (2) is simplified appreciably.

$$E_s(\vec{\mathbf{r}},t) = E_s \gamma_m(\vec{\mathbf{r}}) \exp\left(-i\frac{2\pi}{\lambda} v t n_{\text{air}}\right) \quad \left[\frac{\text{V}}{\text{m}}\right]. \tag{3}$$

This expression introduces the symbol for the MCF, γ_m. Similar to the case in the theory of partial coherence, the MCF is a complex quantity. It, in turn, is a product of the complex container coherence function γ_g and the complex sample coherence functions γ_{si}.

$$\gamma_m(\vec{\mathbf{r}}) = \gamma_g^2 \prod_i \gamma_{s_i}(\vec{\mathbf{r}}). \tag{4}$$

The previous quantities are shown explicitly to depend on the point of probe $\vec{\mathbf{r}}$. It is on the basis of this spatial dependence that both tissue characterization and imaging are to be obtained. On the one hand, we may assume the container characteristics γ_g to be known. On the other hand, sample coherence functions γ_{si} provide the information for diagnosis as shown next.

$$\gamma_g = \sqrt{\mathcal{R}_g} \exp\left(-i\frac{2\pi}{\lambda} n_g d\right), \tag{5}$$

$$\gamma_{s_i}(\vec{\mathbf{r}}) = \exp\left\{-\frac{1}{2}[\mu_{a_i}(\vec{\mathbf{r}}) + \mu_{s_i}(\vec{\mathbf{r}})]D_i(\vec{\mathbf{r}})\right\} \times \exp\left[-i\frac{2\pi}{\lambda} n_{s_i}(\vec{\mathbf{r}}) D_i(\vec{\mathbf{r}})\right]. \tag{6}$$

These coherence functions describe how the attenuation takes place when ballistic photons travel through the sample. For *in vivo* biological samples, the complex container coherence function is equal to Fresnel reflection. Whenever one layer of tissue is analyzed (for instance, in *in vitro* analyses) we may recover the attenuation coefficient describing the sample, by knowing the MCF. For other scenarios, the MCF is an integrated value of attenuation and provides a basis for an imaging approach similar to computed axial tomography. The superposition of reference, Eq. (1), and sample beams, Eq. (3), in the detector plane yields the interference expression as a function of the MCF.

$$P(\vec{\mathbf{r}}_1,t) = P_r + P_s|\gamma_m(\vec{\mathbf{r}}_1)|^2 + 2\sqrt{P_r P_s}|\gamma_m(\vec{\mathbf{r}}_1)| \times \cos\left[\Phi + \Phi_m(\vec{\mathbf{r}}_1) - \frac{2\pi}{\lambda} v t n_{\text{air}}\right] \quad [\text{W}]. \tag{7}$$

Here P_r and P_s denote the power in the reference and sample arms, respectively. The quantities P_r and P_s refer to the total power transmitted on irradiating a small probe area. $|\gamma_m|$ represents the amplitude of the complex material coherence function. The phase of the complex material coherence function is denoted by Φ_m, and Φ encompasses all remaining phase terms. In the last expression, we have omitted the proportionality coefficients relating the electrical field to power. Additionally, we suppose that a specific point of probe is being assessed, $\vec{\mathbf{r}}_1$.

In Eq. (7) we assume that a coherent source is employed. Hence the amplitude of the function of self-coherence is omitted. Furthermore, this expression applies to the transmitted pass-through field. To put it another way, this relation is valid only when no scattering centers are included in the sample, as for instance, in mostly absorbing tissues. However, when scattering centers are present, a more detailed analysis is necessary. In such a case, the interferometric experiment may be represented schematically as shown in Fig. 2.

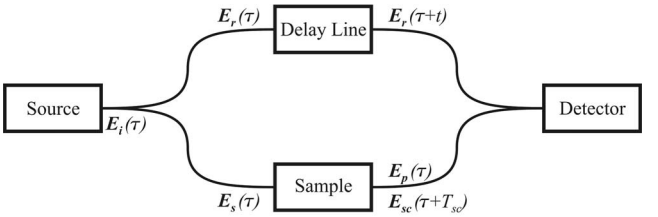

Fig. 2 Schematic representation of the interferometric setup depicting the emergence of commingled scattered and ballistic photons.

For a specific probe point, different interactions may be observed in the detection plane. First, we expect to measure a deterministic offset. Such a term corresponds to the amount of reference E_r and pass-through E_p photons that arrive to the detection plane. Second, a stochastic term analogous to the former two will ensue. It represents the signal that the forward-scattered E_{sc} radiation produces. Third, a random dc signal will appear because the scattered and pass-through photons retain a certain degree of coherence after traversing the tissue. Fourth, the pass-through and reference photons will generate a temporal variation of the irradiance. Finally, a fifth term will result. It is a stochastically varying function due to the interaction between scattered and reference photons. These interactions may be described as shown in Eq. (8).

$$\begin{aligned} P(t,T_{sc}) \propto\ & \langle E_r^*(\tau+t)E_r(\tau+t)\rangle + \langle E_p^*(\tau)E_p(\tau)\rangle \\ & + \langle E_{sc}^*(\tau+T_{sc})E_{sc}(\tau+T_{sc})\rangle + \langle E_p^*(\tau)E_{sc}(\tau+T_{sc})\rangle \\ & + \langle E_{sc}^*(\tau+T_{sc})E_p(\tau)\rangle + \langle E_r^*(\tau+t)E_p(\tau)\rangle \\ & + \langle E_p^*(\tau)E_r(\tau+t)\rangle + \langle E_r^*(\tau+t)E_{sc}(\tau+T_{sc})\rangle \\ & + \langle E_{sc}^*(\tau+T_{sc})E_r(\tau+t)\rangle \quad [\text{W}]. \end{aligned} \tag{8}$$

Here P is the detected power. τ represents the time delay taken as reference, and t is the modulation time induced by the delay line. The extra (random) time that the scattered photons take to traverse the sample, due to multiple interactions of radiation with tissue, is described by T_{sc}. The chevrons denote time average and an asterisk demarcates complex conjugation.

To arrive at the model describing the experiment, we need to relate the reference E_r and sample E_s beams to the incident electrical field of the source E_i. The relation between reference and incident beams is easy to obtain. They depend only on splitting factors of the beam dividers in the interferometer. In contrast, the relation between sample and incident beams is not as straightforward. On the one hand, we have introduced the concept of complex material coherence function to relate the emerging pass-through field to the incident sample beam.

$$E_p(\vec{\mathbf{r}},\tau)=\gamma_m(\vec{\mathbf{r}})E_s(\vec{\mathbf{r}},\tau)\quad\left[\frac{\mathrm{V}}{\mathrm{m}}\right]. \tag{9}$$

On the other hand, no simple expression exists to associate the forward-scattered field with the incident one. This happens because radiation interaction with tissue is a stochastic process. However, due to energy conservation, the scattered and incident fields are related to each other. We represent such relation by introducing a complex scattering coherence function $\gamma_{sc}(\vec{\mathbf{r}},T_{sc})$.

$$E_{sc}(\vec{\mathbf{r}},\tau+T_{sc})=\gamma_{sc}(\vec{\mathbf{r}},T_{sc})E_s(\vec{\mathbf{r}},\tau)\quad\left[\frac{\mathrm{V}}{\mathrm{m}}\right]. \tag{10}$$

It is important to understand that although this expression looks simple, the complex scattering coherence function is a stochastic function. Therefore, analytical descriptions of the same are intricate. Once again, if we assume that a certain pixel (i.e., spatial area) is being assessed, we may drop the spatial dependence of the last equations. Furthermore, if we denote the splitting coefficients of the beam dividers as k_{sp1} and k_{sp2}, we can express the superposition of fields in terms of the incident field.

$$\begin{aligned}P(t,T_{sc})\propto{}&(1-k_{sp1})(1-k_{sp2})\langle E_i^*(\tau+t)E_i(\tau+t)\rangle+k_{sp1}k_{sp2}\\&\times\{|\gamma_m|^2\langle E_i^*(\tau)E_i(\tau)\rangle+|\gamma_{sc}|^2\langle E_i^*(\tau+T_{sc})E_i(\tau+T_{sc})\rangle\\&+|\gamma_m||\gamma_{sc}|[\langle E_i^*(\tau)E_i(\tau+T_{sc})\rangle+\langle E_i^*(\tau+T_{sc})E_i(\tau)\rangle]\}\\&+\sqrt{k_{sp1}}\sqrt{1-k_{sp1}}\sqrt{k_{sp2}}\sqrt{1-k_{sp2}}\\&\times\{|\gamma_m|[\langle E_i^*(\tau+t)E_i(\tau)\rangle+\langle E_i^*(\tau)E_i(\tau+t)\rangle]\\&+|\gamma_{sc}|[\langle E_i^*(\tau+t)E_i(\tau+T_{sc})\rangle\\&+\langle E_i^*(\tau+T_{sc})E_i(\tau+t)\rangle]\}\quad[\mathrm{W}].\end{aligned} \tag{11}$$

In this expression, we introduce the temporal dependence of the scattering coherence function as a phase term T_{sc} in the corresponding electrical field. The phase modulation t is also included. We further note that the interferogram is composed of deterministic and stochastic dc terms. In addition, the amplitude of the modulated signals fluctuates either randomly or predictably. From Eq. (11), the application of partial coherence theory follows.

$$\begin{aligned}P(t,T_{sc})=\Gamma_{i,i}(0)&((1-k_{sp1})(1-k_{sp2})+k_{sp1}k_{sp2}\\&\times\{|\gamma_m|^2+|\gamma_{sc}|^2+2|\gamma_m||\gamma_{sc}||\gamma_{i,i}(T_{sc})|\cos[\Phi_{i,i}(T_{sc})]\}\\&+2\sqrt{k_{sp1}}\sqrt{1-k_{sp1}}\sqrt{k_{sp2}}\sqrt{1-k_{sp2}}\\&\times\{|\gamma_m||\gamma_{i,i}(t)|\cos[\Phi_{i,i}(t)]\\&+|\gamma_{sc}||\gamma_{i,i}(t+T_{sc})|\cos[\Phi_{i,i}(t+T_{sc})]\})\quad[\mathrm{W}].\end{aligned} \tag{12}$$

Here, $\Gamma_{i,i}(0)$ represents the optical incidance[49] (or total collected power on proving a small area), which includes the proportionality coefficient relating the electrical field to power. $|\gamma_{i,i}(\tau)|$ represents the amplitude of the complex degree of self-coherence. The phase of the complex degree of self-coherence is denoted by $\Phi_{i,i}(\tau)$.

The representation by partial coherence theory facilitates the interpretation of the detected signal. The first two terms are the deterministic offset. Furthermore, they correspond to the amount of reference and pass-through photons that arrive to the detection plane. The next term is analogous to the former two but it is stochastic. It represents the dc signal that the forward-scattered radiation induces. The fourth term is more intricate. It stands for the interference that pass-through and forward-scattered photons produce due to the late arrival of the latter. The last two terms constitute the temporally modulated interference between pass-through and reference beams and between forward-scattered and reference beams. We are interested in the first modulated quantity to perform analysis. Nonetheless, forward-scattered radiation is entangled with the pass-through because the former arrives promptly after the latter.

The first step in the recovery of information, necessary for diagnosis, is to eliminate the fluctuating offset. In a recent publication, we proposed to use phase-locked detection to isolate the signal.[50] However, lock-in amplifiers require a stable reference signal for adequate performance. Considering that in our experimental setup the temporal modulation is generated by an open-loop nanopositioning system, phase-locked detection is not the optimal filter. Instead, we employ a high-pass electrical filter to eliminate the terms. After dc filtering, the measured signal is composed solely of temporally modulated signals.

$$\begin{aligned}P(t,T_{sc})=\Gamma_{i,i}(0)&(2\sqrt{k_{sp1}}\sqrt{1-k_{sp1}}\sqrt{k_{sp2}}\sqrt{1-k_{sp2}}\\&\times\{|\gamma_m||\gamma_{i,i}(t)|\cos[\Phi_{i,i}(t)]\\&+|\gamma_{sc}||\gamma_{i,i}(t+T_{sc})|\cos[\Phi_{i,i}(t+T_{sc})]\})\quad[\mathrm{W}].\end{aligned} \tag{13}$$

From this expression, we observe that if the coherence time of the source is less than the expected time of flight for scattered radiation T_{sc}, the latter will not be detected. A clarification is relevant here. When we speak of the time of coherence of the source, we are referring to a specific measure. Well-established biomedical techniques, such as optical coherence tomography (OCT), take as time of coherence the full width at half maximum (FWHM) of the amplitude of the function of self-coherence.[51] For our purposes this is not sufficient, as is explained shortly. Instead, the definition of coherence time as introduced by Mandel is adequate for our analysis.[52]

$$\tau_c=4\int_0^\infty|\gamma_{i,i}(t)|^2\mathrm{d}t\quad[\mathrm{s}]. \tag{14}$$

The assessment of Eq. (14), assuming a Gaussian power spectral density, yields the coherence time τ_c for many commercial radiation sources.

$$\tau_c=2\sqrt{\frac{2\ln(2)}{\pi}}\frac{\bar{\lambda}^2}{c\Delta\lambda}\quad[\mathrm{s}]. \tag{15}$$

Here $\bar{\lambda}$ represents the central wavelength of emission. $\Delta\lambda$ is the bandwidth (at FWHM) of the source and c stands for the velocity of light in vacuum.

We know that scattering is dominant in radiation-tissue interactions.[53] Therefore, we need to filter effectively, such radiation. Substituting the coherence time, defined in Eq. (15), into the corresponding amplitude of the function of self-coherence unveils a reduction of three orders of magnitude, $|\gamma_{i,i}(\tau_c)|=1.87\times10^{-3}$. A comparison between this value and

that of OCT, $|\gamma_{i,i}(\tau_c=\tau_{\mathrm{OCT}})|=0.5$, emphasizes the appropriateness of using Eq. (14) for filtering purposes. Taking this information into account, we may conclude that any photon arriving at a time greater than the coherence time of the source will be filtered out efficiently. This is relevant for the calibration procedure of the instrument, because radiation sources will behave differently depending on their coherence characteristics. For further details on the coherence analysis (including comparisons between different radiation sources), we refer the reader to a recent publication of our group.[50] If we assume that the coherence filter serves its purpose successfully, the temporal maxima of Eq. (13) yield a proportional measure of the sought information.

$$\max\{P(t)\}=2\Gamma_{i,i}(0)\sqrt{k_{sp1}}\sqrt{1-k_{sp1}}\sqrt{k_{sp2}}\sqrt{1-k_{sp2}}|\gamma_m| \quad [\mathrm{W}]. \tag{16}$$

For *in vitro* studies, the contributions of the sample container are undesired. Hence we need a means to discard such information. To achieve this, we may normalize the measurements by calculating Eq. (16), while including as a sample a transparent liquid (i.e., nonscattering) with a similar index of refraction as the tissue under test. In the next section, we elaborate further on normalization issues, while describing in detail the experimental setup built to validate pass-through photon-based biomedical transillumination.

3 Materials and Methods

3.1 *Experimental Setup*

In the transillumination interferometer depicted in Fig. 1, the radiation traverses the sample under test only once. This is most desirable because the process under study is exponential, as illustrated in Eq. (2), and power decreases rapidly. However, we prefer to work with a Michelson configuration to confirm the viability of the concept. Although in this setup the radiation must traverse the sample twice, the interferometer benefits from other important characteristics such as ease of compensation and lack of misalignments (during temporal modulation). Nonetheless, after the concept has been successfully validated in a traditional Michelson system, a fiber-optic-based Mach-Zehnder implementation will enhance overall performance. In Fig. 3 we show a schematic layout of the partial coherence Michelson interferometer.

The emphasis of this analysis is placed on the validation of pass-through photon-based transillumination. In the theory part of this work, we established that coherence filtering plays an important role for ensuring isolated detection of ballistic photons. Nevertheless, low-coherence sources exhibit coherence lengths in orders of microns (10^1 to 10^2 μm), and thus detection of co-mingled pass-through and single scattered radiation may ensue. This happens because single scattering solely modifies the direction of propagation of light. Therefore, to minimize detection of scattered radiation, we carefully implement three features in our experiment.

First, we collimate the radiation source conscientiously to ensure a maximum optical length with the same transversal spot size. Second, we build the interferometer compactly so that the radiation traverses the sample directly after having left the collimation optics. Third, we place the detection plane distant from the sample to permit spatial divergence of scattered photons. It is then important to recognize that spot size not only determines pixel size in our experiment, but also the region where optical noise may be found. Hence for optimal performance of the system, small pixel sizes could be preferable. Figure 4 is a photograph of the experimental setup, as implemented in our laboratory, where the aforementioned features may be recognized.

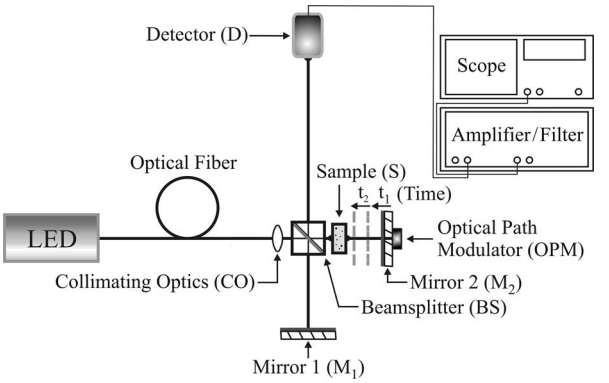

Fig. 3 Schematic layout implemented to validate pass-through photon-based transillumination interferometry for biomedical applications. The sample arm is modulated (t_1, t_2, etc.) to generate an interferogram.

Several remarks concerning the experimental implementation are in order here. The partial coherence source is a fiber-coupled LED (637-nm central wavelength, 20-nm FWHM, 25-mW output power, and 0.47 N.A., WT and T Incorporated, Pierrefonds, Canada) with a coherence length of approximately 27 μm, as calculated from Eq. (15). Due to the large numerical aperture of the source, several optical components are utilized to collimate the radiation. Furthermore, the tradeoff between collimated power and diameter of collimation restricts us to a 7 to 8-mm-wide beam with approximately 500 μW. This value places a tight demand on the detection electronics because of the expected exponential decay of power. To improve this condition, an increment on the incident power of approximately one order of magnitude may ensue. With such an increment, we would still comply with safety considerations, such as those of ANSI standards.[54] Another aspect that may be improved is the pixel size. The proof of concept does not require a compact pixel size. However,

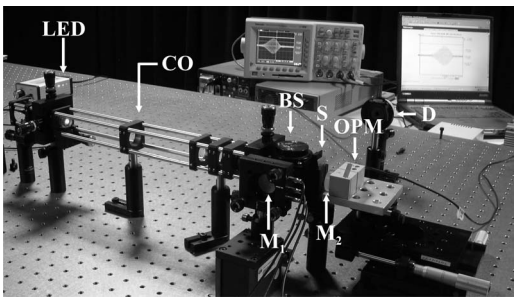

Fig. 4 Pass-through photon-based transillumination interferometer in a Michelson configuration. The letters are the same as used in Fig. 3. LED is light emitting diode, CO is collimating optics, BS is the beamsplitter, S is the sample, M_1 is mirror 1, M_2 is mirror 2, OPM is the optical path modulator, and D is the detector.

Table 1 Equivalent volumetric and percentage concentrations of tissue phantom assessed in the experiment.

Volumetric [μl/μl]	$\frac{1.25}{1000}$	$\frac{2.50}{1000}$	$\frac{3.75}{1000}$	$\frac{5.00}{1000}$	$\frac{6.25}{1000}$	$\frac{7.50}{1000}$	$\frac{8.75}{1000}$	$\frac{10.00}{1000}$	$\frac{11.25}{1000}$	$\frac{12.50}{1000}$
Percentage [%]	0.125	0.250	0.375	0.500	0.625	0.750	0.825	1.000	1.125	1.250

for applications such as tissue characterization, spatial extent is important. The utilization of a super luminescent diode (SLED) would be capable of providing both power and compact pixel size.

The temporal modulator is of central importance for the system. This is because by finding the maximum of the signal, we need not consider the effects introduced by the amplitude of the function of self-coherence. However, whenever a different sample is introduced in the interferometer, the system must be compensated accordingly. In the experimental setup, we utilize a nanopositioning system with a 100 μm travel. We limit the effective travel of the modulator to 50 μm, because in the current experiment we do not expect large optical path differences. In addition, we center the modulator such that the maximum of the function of self-coherence is located in the middle of the travel range. This is relevant, since the nanopositioning system works in an open-loop regime, and hence exhibits hysteresis. The most detrimental effects of hysteresis appear at the beginning (or end) of each travel, and thus do not influence the output of the interferometer. Nevertheless, a system with closed-loop control would serve to enable phase-locked detection with the implicit benefits it provides.

Tissue exhibits marked attenuation properties while interacting with light, such that ballistic photons are rare events. Therefore, in the experimental setup, we utilize a 1-mm-thick cuvette as a sample holder. The attenuating behavior also serves to demarcate the kind of tissues that may be analyzed with the technique. At present, we foresee dental tissue as a plausible sample for pass-through photon-based transillumination.

3.2 *Materials*

The phenomenon under study exhibits an exponential decay and hence must be characterized with detail. For this reason, we prepared several concentrations of a well-established tissue phantom. We utilize a sample that displays marked characteristics of scattering because absorption is solely observed as a decrease in optical power. Meanwhile, scattering is present throughout the experiment and is difficult to overcome, because scattered radiation in tissues is predominantly forward directed.[55] Thus we employ a sample exhibiting marked scattering characteristics to evaluate the feasibility of pass-through photon-based transillumination.

We utilize a lipid-based emulsion consisting of Lipofundin™ 10% (B. Braun Melsungen Laboratory, Melsungen, Germany) and distilled water. The phantom material (marketed trade names Intralipid™, Nutralipid™, or Lipofundin™) is a reproducible source of lipids. Its stability is better than 10%, and successful reuse of the emulsion has been reported over many days.[56] An additional relevant feature of these lipid-based phantoms is their reliability for studies with visible radiation.[57] This convenience facilitates the alignment and experimental procedures. For final clinical purposes, we would take advantage of the optimal therapeutic window in the near-IR to perform diagnosis.[58–60]

We prepare ten samples by increasing the concentration of the tissue phantom gradually and meticulously. The use of a micropipette (Finnpipette 4500050, Thermo Scientific) ensures the accuracy of the emulsions. Assuming that the total volume of the sample is 1000 μl, the increment of the (equivalent) volumetric concentrations of the tissue phantom employed is 1.25 μl. Hence the assessed range of sample concentration spans the values utilized conventionally to mimic tissue-like optical properties with a lipid emulsion like Lipofundin™, as shown in Table 1.

It is important to keep in mind that in the Michelson interferometer, the sample behaves as a tissue of two-fold concentration due to the double pass implicit in the configuration. Hence the results obtained are valid for samples two times more attenuating in a Mach-Zehnder interferometer.

3.3 *Methods*

Concerning the methodology employed during the experiment, we would like to point out the importance of normalizing the measurements. In Eq. (16), a proportional measure of the quantity of interest is proposed. Nonetheless, such a measure is also influenced by features of the instrument (e.g., splitting factors, detector responsivity, etc.). To cancel out these effects, we perform a normalization of the measurements. This procedure improves further the reliability of the technique, since the stability of the measurements does not have to span the complete experiment. Indeed, stability during measurements with sample and with reference (i.e., normalization) setups suffices for obtaining consistent results.

As singled out previously, for *in vitro* experiments, a transparent sample with similar index of refraction as the sample of interest may be utilized to normalize the measurements. In this case, the material coherence function, Eq. (4), would be composed solely of the container coherence function. Therefore, the normalized measurements would not include information related to the sample holder. The case of *in vivo* studies is different. In such scenarios, we propose to cancel out all factors associated with the instrument, leaving only the information related to the material coherence function. To achieve this, the reference setup would not include a sample in the interferometer arm. Thus, the normalized measurements would only reveal information pertaining to the tissue under test.

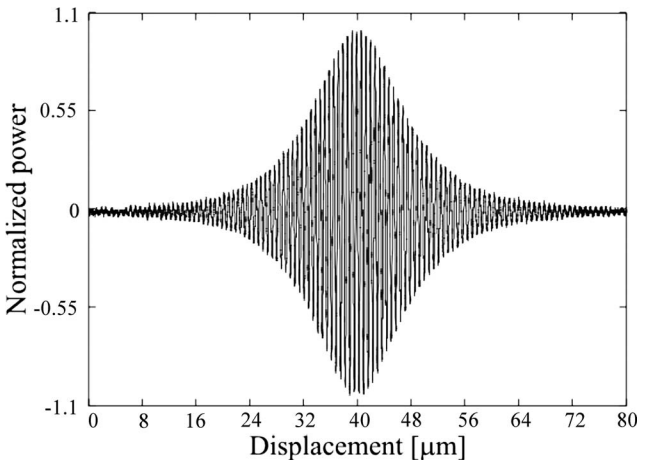

Fig. 5 The response of the partial coherence transillumination interferometer without sample is symmetric due to the quality of the optical components.

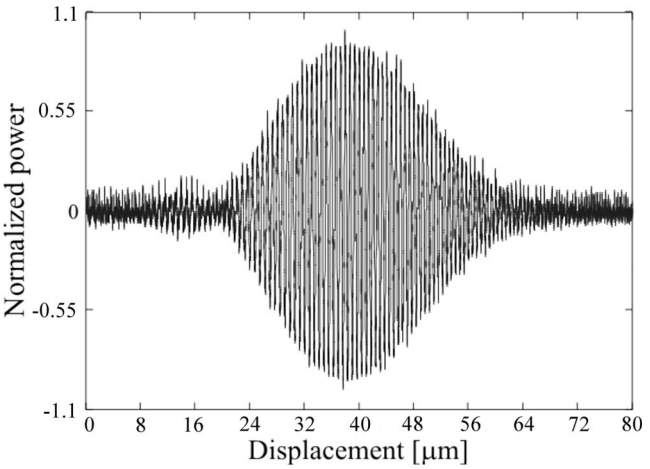

Fig. 6 The response of the partial coherence transillumination interferometer with reference sample is asymmetric due to the inclusion of the sample holder.

Before presenting the experimental results we would like to briefly describe the methodology followed during measurements. First, the partial coherence interferometer without a sample is aligned and compensated. For *in vivo* studies, we need to ensure that finding this position is rapid and reliable. Furthermore, depending on the extent of the sample under test, this endeavor may be somewhat complicated. Whenever the interferometer is in optimal conditions, the reference measurement is taken for *in vivo* studies. In contrast, for *in vitro* analyses the sample holder is introduced with a transparent sample (distilled water, in our case), and the reference measurement is taken. It is important to keep in mind that most sample holders are not designed for interferometric applications. Therefore, the importance of canceling the effects of the container by normalizing the measurements.

Next, the sample is introduced in one arm of the interferometer. In the case of *in vivo* studies, the interferometer is compensated accordingly. For *in vitro* analyses, the optical path difference will not affect appreciably the performance of the instrument. Nonetheless, for this to be the case, the displacement of the optical path modulator is of significant importance. Finally, amplifier and detection electronics are set depending on the attenuating characteristics of the tissue, and the sample measurement is taken. With this idea in mind, we now present and discuss our experimental results.

4 Results and Discussion

We have mentioned throughout the work that adequate normalization of measurements is desirable. In what follows, we would like to demonstrate that this is the case. To arrive at this conclusion, we first align and compensate the partial coherence interferometer. After alignment and compensation, the behavior of the system is known: an amplitude modulated sinusoidal response. The amplitude modulation is given by the envelope of the self-coherence function. The inclusion of a sample holder with a transparent medium should not affect, in theory, the quality of the interferogram. However, if the optical quality of the container is distant from interferometric class, performance of the system deteriorates. In Figs. 5 and 6, we compare the performance of the interferometer without sample and with the reference liquid (i.e., distilled water).

The importance of adequate normalization is evident from Figs. 5 and 6. Furthermore, by ensuring interferometric quality of the sample container, we predict a behavior like the one depicted in Fig. 5. However, for daily routine *in vitro* measurements, interferometric-class containers are not viable, hence the importance of adequately compensating sample holder effects.

Now we address the proof of concept for pass-through photon-based transillumination interferometry for biomedical applications. As stated in the previous section, we prepared a series of tissue phantoms with increasing attenuating characteristics. In Figs. 7 and 8, we show the corresponding interferometric measurements for the tissue phantom composed of a $2.5/1000\ [\mu l/\mu l]$ concentration and the corresponding signal for the reference sample (distilled water).

The signals in Figs. 7 and 8 serve to recognize the expected attenuating characteristics of the sample. Regardless of

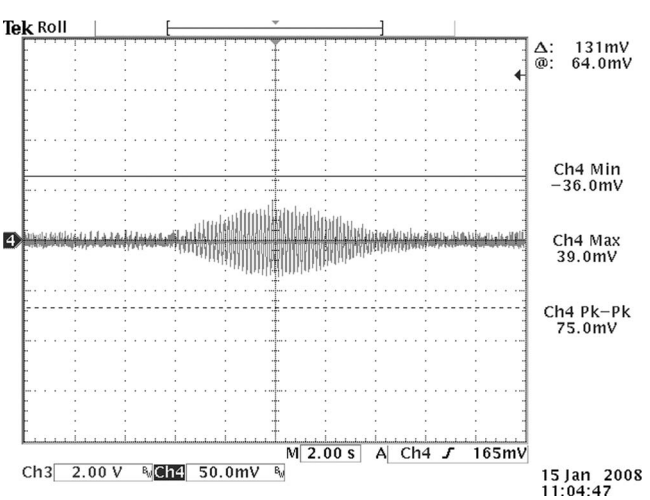

Fig. 7 Representative interference signal for one of the scattering concentrations: $2.5/1000\ [\mu l/\mu l]$.

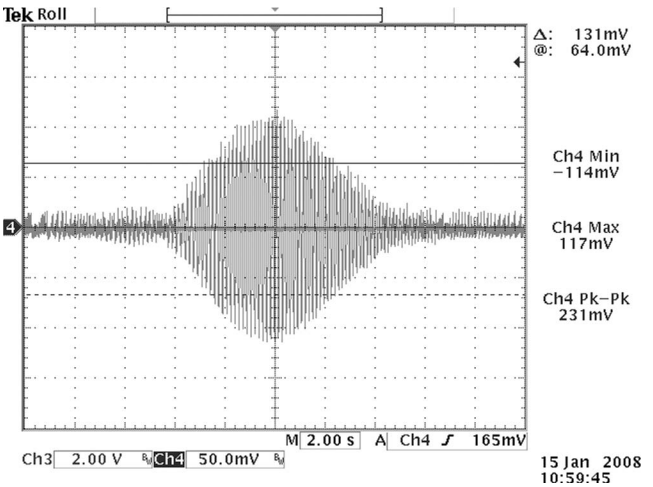

Fig. 8 Corresponding reference signal for normalizing the measurements of the sample of Fig. 7.

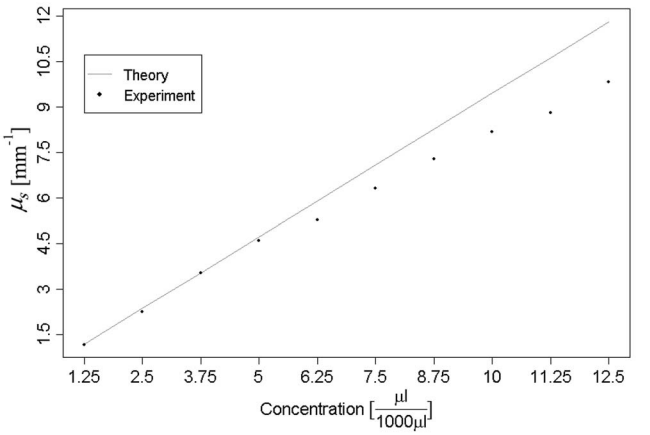

Fig. 10 Theoretical and experimental comparison of the scattering coefficients for Lipofundin™ 10%.

having a relatively low scattering concentration, the signal decreases three-fold. Now, the aim of the analysis is to recover the material coherence function for a certain tissue (phantom) from interferometric measurements, such as those depicted in Figs. 7 and 8. Equation (16) yields a proportional measure of the amplitude of the material coherence function. If normalization is performed, the effects of the container are canceled out, and the results correspond solely to the amplitude of the sample coherence function, as may be verified in Eq. (4). Therefore, we expect to observe an exponential decay as concentration is increased. In Fig. 9, we present the experimental results for the tissue phantom concentrations listed in Table 1.

In Fig. 9 we have omitted the error bars of the volumetric concentrations for ease of reading. The accuracy of the micropipette is better than 1%, and as such, the error bars are close together. Nonetheless, the error bars of the x axis may be incorporated by modifying our statistical program, coded in R.[61,62] Furthermore, the error bars of the y axis correspond to electronic fluctuations during measurements. The standard deviation of the maximum and (absolute) minimum values for ten modulation cycles is considered. Greater error bars are due to measurements directly from the oscilloscope display and may be reduced by signal downloading and offline processing.

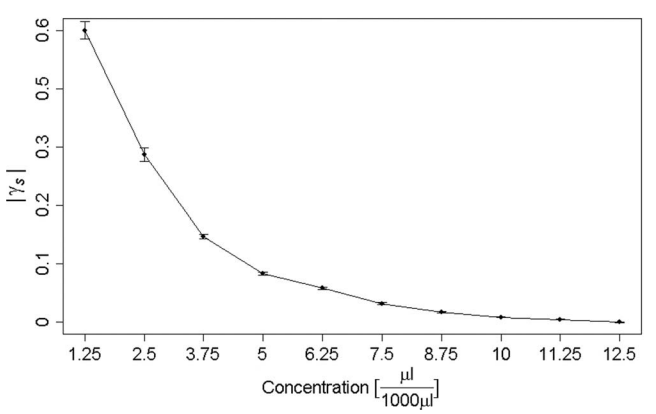

Fig. 9 The amplitude of the sample coherence function, for the tissue phantom under study, exhibits an exponential behavior as predicted in Eq. (6).

The exponential behavior of the sample coherence function is manifest in the graphic representation of Fig. 9. As described in Sec. 3, the sample is composed of one layer of a well-established tissue phantom. Therefore, we may recover the corresponding scattering coefficients by using the data depicted in Fig. 9 and Eq. (6). Furthermore, assuming that the tissue phantom behaves similarly to Intralipid™, the theoretical scattering coefficients may be calculated from the expressions due to van Staveren et al.[57] It is important to keep in mind that theoretical scattering coefficients for samples of two-fold concentration must be calculated, because the radiation traverses the phantom twice. In Fig. 10, we show a comparative plot of such theoretical coefficients and the experimental values obtained in this work.

In Fig. 10, we observe good agreement between theory and experiment for the initial set of samples. As scatterer concentration increases, the presence of (optical) noise becomes more prominent. The use of either a spatially compact source or a minimally divergent beam would help to counteract this phenomenon. Nonetheless, we may conclude that pass-through photon-based transillumination interferometry, for selected biomedical applications, is feasible.

5 Conclusion and Outlook

The implementation of pass-through photon-based transillumination depends on tissue under test, power, spatial and spectral characteristics of the radiation source, and detection electronics. The importance of matching power, detection electronics, and adequate tissue extent is recognizable because the process under study is exponential. Therefore, an accurate calibration between detector, radiation power, and sample is necessary to ensure performance. Furthermore, the spectral signature of the source is underlined as relevant for the technique. Despite coherence lengths being on the orders of microns, detection of commingled pass-through and single scattered radiation may ensue. In the case of scattered photons, a spatially compact radiation source provides a means to over-

come optical noise. Furthermore, a displacement of the detection plane improves the filtering of scattered radiation.

Pass-through photon-based transillumination may become an alternative for tissue characterization and diagnosis, for instance, of dental samples. For *in vitro* and *in vivo* applications, we have described normalization procedures that are advisable. In the former case, a choice of a transparent liquid that mimics the index of refraction of the sample would serve to eliminate container-related characteristics. This is most important when the recipient is not of interferometric quality. Considering the latter application, instrument-related quantities may be canceled out by normalizing the measurements with respect to a system without sample.

The proposed measure for diagnosis, the material coherence function, describes the characteristics of the sample to decrease the degree of coherence of a coherent beam on its passing through it. Whenever one layer of tissue is analyzed (for instance, in *in vitro* analyses), we may recover the attenuation coefficient for tissue characterization purposes by knowing the material coherence function. For other scenarios, the material coherence function is an integrated value of attenuation and provides a basis for an imaging approach similar to computed axial tomography.

In this work, we determined the sample coherence function of a tissue phantom, and from this information, the corresponding scattering (i.e., attenuation) coefficients were determined. For the initial set of samples, good agreement between theory and experiment served to conclude that pass-through photon-based transillumination is feasible for selected biomedical applications.

Nonetheless, we must also underline that several improvements await implementation. First, a more robust fiber-based Mach-Zehnder interferometer must be built. Second, a SLED may serve to improve important features such as power, pixel size, and beam collimation. Third, a closed-loop modulator would facilitate the use of a lock-in amplifier with the implicit benefits it provides.

Acknowledgment

Paulino Vacas-Jacques gratefully acknowledges the National Science and Technology Foundation of Mexico (CONACyT) for financial support, grant 172068.

References

1. M. Salvetti, M. L. Muiesan, A. Paini, C. Monteduro, B. Bonzi, G. Galbassini, E. Belotti, E. Movilli, G. Cancarini, and E. Agabiti-Rosei, "Myocardial ultrasound tissue characterization in patients with chronic renal failure," *J. Am. Soc. Nephrol.* **18**(6), 1953–1958 (2007).
2. C. W. Sun, Y. M. Wang, L. S. Lu, C. W. Lu, I. J. Hsu, M. T. Tsai, C. C. Yang, Y. W. Kiang, and C. C. Wu, "Myocardial tissue characterization based on a polarization-sensitive optical coherence tomography system with an ultrashort pulsed laser," *J. Biomed. Opt.* **11**(5), 054016 (2006).
3. D. Huang, E. Swanson, C. Lin, J. Schuman, W. Stinson, W. Chang, M. Hee, T. Flotte, K. Gregory, C. Puliafito, and J. Fujimoto, "Optical coherence tomography," *Science* **254**, 1178–1181 (1991).
4. E. Swanson, D. Huang, M. Hee, J. Fujimoto, C. Lin, and C. Puliafito, "High-speed optical coherence domain reflectometry," *Opt. Lett.* **17**(2), 151–153 (1992).
5. S. Chinn, E. Swanson, and J. Fujimoto, "Optical coherence tomography using a frequency-tunable optical source," *Opt. Lett.* **22**(5), 340–342 (1997).
6. G. Tearney, B. Bouma, and J. Fujimoto, "High-speed phase- and group-delay scanning with a grating-based phase control delay line," *Opt. Lett.* **22**(23), 1811–1813 (1997).
7. H. Hiratsuka, E. Kido, and T. Yoshimura, "Simultaneous measurements of three-dimensional reflectivity distributions in scattering media based on optical frequency-domain reflectometry," *Opt. Lett.* **23**(18), 1420–1422 (1998).
8. M. Wojtkowski, V. Srinivasan, T. Ko, J. Fujimoto, A. Kowalczyk, and J. Duker, "Ultrahigh-resolution, high-speed, Fourier domain optical coherence tomography and methods for dispersion compensation," *Opt. Express* **12**(11), 2404–2422 (2004).
9. E. Choi, J. Na, S. Ryu, G. Mudhana, and B. Lee, "All-fiber variable optical delay line for applications in optical coherence tomography: feasibility study for a novel delay line," *Opt. Express* **13**(4), 1334–1345 (2005).
10. B. Vakoc, S. Yun, J. de Boer, G. Tearney, and B. Bouma, "Phase-resolved optical frequency domain imaging," *Opt. Express* **13**(14), 5483–5493 (2005).
11. A. Tumlinson, J. Barton, B. Povazay, H. Sattman, A. Unterhuber, R. Leitgeb, and W. Drexler, "Endoscope-tip interferometer for ultrahigh resolution frequency domain optical coherence tomography in mouse colon," *Opt. Express* **14**(5), 1878–1887 (2006).
12. A. E. Desjardins, B. J. Vakoc, A. Bilenca, G. J. Tearney, and B. E. Bouma, "Estimation of the scattering coefficients of turbid media using angle-resolved optical frequency-domain imaging," *Opt. Lett.* **32**(11), 1560–1562 (2007).
13. G. Paez, M. Strojnik, and M. Scholl, "Interferometric tissue characterization: I. Theory," *Proc. SPIE* **5883**, 58830Y (2005).
14. G. Paez, M. Strojnik, and S. Scholl, "Interferometric tissue characterization: IV. Material coherence function," *Proc. SPIE* **5883**, 58830X (2005).
15. M. Strojnik and G. Paez, "Interferometric tissue characterization: II. Experimental," *Proc. SPIE* **5883**, 58830W (2005).
16. P. Vacas-Jacques, M. Strojnik, and G. Paez, "Transmission profile function reconstruction for complex transmission interferometry: biomedical applications," *Proc. SPIE* **6307**, 63070P (2006).
17. M. Strojnik and G. Paez, "Interferometric tissue characterization: III. Calibration," *Proc. SPIE* **5883**, 58830V (2005).
18. P. Vacas-Jacques, M. Strojnik, and G. Paez, "Reduced coherence and calibration optimization for transillumination interferometry," *Proc. SPIE* **6429**, 64292K (2007).
19. S. Andersson-Engels, R. Berg, S. Svanberg, and O. Jarlman, "Time-resolved transillumination for medical diagnostics," *Opt. Lett.* **15**(21), 1179–1181 (1990).
20. L. Wang, P. Ho, C. Liu, G. Zhang, and R. Alfano, "Ballistic 2-D imaging through scattering walls using an ultrafast optical Kerr gate," *Science* **253**, 769–771 (1991).
21. D. Papaioannou, G. Hooft, J. Baselmans, and M. van Gemert, "Image quality in time-resolved transillumination of highly scattering media," *Appl. Opt.* **34**(27), 6144–6157 (1995).
22. G. Le Tolguenec, F. Devaux, and E. Lantz, "Two-dimensional time-resolved direct imaging through thick biological tissues: a new step toward noninvasive medical imaging," *Opt. Lett.* **24**(15), 1047–1049 (1998).
23. M. Hee, J. Izatt, J. Jacobson, J. Fujimoto, and E. Swanson, "Femtosecond transillumination optical coherence tomography," *Opt. Lett.* **18**(12), 950–952 (1993).
24. M. Hee, J. Izatt, E. Swanson, and J. Fujimoto, "Femtosecond transillumination tomography in thick tissues," *Opt. Lett.* **18**(13), 1107–1109 (1993).
25. D. Grosenick, H. Wabnitz, and H. Rinneberg, "Time-resolved imaging of solid phantoms for optical mammography," *Appl. Opt.* **36**(1), 221–231 (1997).
26. D. Grosenick, H. Wabnitz, H. H. Rinneberg, K. T. Moesta, and P. M. Schlag, "Development of a time-domain optical mammography and first in vivo applications," *Appl. Opt.* **38**(13), 2927–2943 (1999).
27. D. Grosenick, K. T. Moesta, H. Wabnitz, J. Mucke, C. Stroszczynski, R. Macdonald, P. M. Schlag, and H. Rinneberg, "Time-domain optical mammography: initial clinical results on detection and characterization of breast tumors," *Appl. Opt.* **42**(42), 3170–3186 (2003).
28. H. P. Chiang, W. S. Chang, and J. Wang, "Imaging through random scattering media by using cw broadband interferometry," *Opt. Lett.* **18**(7), 546–548 (1993).

29. S. G. Demos and R. R. Alfano, "Temporal gating in highly scattering media by the degree of optical polarization," *Opt. Lett.* **21**(2), 161–163 (1996).
30. X. Liang, L. Wang, P. P. Ho, and R. R. Alfano, "Time-resolved polarization shadowgrams in turbid media," *Appl. Opt.* **36**(13), 2984–2989 (1997).
31. G. Popescu and A. Dogariu, "Ballistic attenuation of low-coherence optical fields," *Appl. Opt.* **39**(25), 4469–4472 (2000).
32. C. W. Sun, K. C. Liu, Y. M. Wang, H. H. Wang, Y. W. Kiang, H. K. Liu, and C. C. Yang, "Determination of target depth in a turbid medium with polarization-dependent transmitted signals," *J. Opt. Soc. Am. A* **20**(11), 2106–2112 (2003).
33. C. W. Sun, C. C. Yang, and Y. W. Kiang, "Optical imaging based on time-resolved Stokes vectors in filamentous tissues," *Appl. Opt.* **42**(4), 750–754 (2003).
34. J. R. Lakowicz and K. Berndt, "Frequency-domain measurements of photon migration in tissues," *Chem. Phys. Lett.* **166**(3), 246–252 (1990).
35. M. S. Patterson, J. D. Moulton, B. C. Wilson, K. W. Berndt, and J. R. Lakowicz, "Frequency-domain reflectance for the determination of the scattering and absorption properties of tissue," *Appl. Opt.* **30**(31), 4474–4476 (1991).
36. J. B. Fishkin and E. Gratton, "Propagation of photon-density waves in strongly scattering media containing an absorbing semi-infinite plane bounded by a straight edge," *J. Opt. Soc. Am. A* **10**(1), 127–140 (1993).
37. B. J. Tromberg, L. O. Svaasand, T. T. Tsay, and R. C. Haskell, "Properties of photon density waves in multiple-scattering media," *Appl. Opt.* **32**(4), 607–616 (1993).
38. M. A. Franceschini, K. T. Moesta, S. Fantini, G. Gaida, E. Gratton, H. Jess, W. W. Mantulin, M. Seeber, P. M. Schlag, and M. Kaschke, "Frequency-domain techniques enhance optical mammography: initial clinical results," *Proc. Natl. Acad. Sci. U.S.A.* **94**(12), 6468–6473 (1997).
39. J. Bai, T. Gao, K. Ying, and N. Chen, "Locating inhomogeneities in tissue by using the most probable diffuse path of light," *J. Biomed. Opt.* **10**(2), 024024 (2005).
40. D. Piao and B. W. Pogue, "Rapid near-infrared diffuse tomography for hemodynamic imaging using a low-coherence wideband light source," *J. Biomed. Opt.* **12**(1), 014016 (2007).
41. M. Toida, M. Kondo, T. Ichimura, and H. Inaba, "Experimental verification of image detection in highly scattering media using antenna properties of optical heterodyne microscope scheme," *Electron. Lett.* **26**(11), 700–702 (1990).
42. K. P. Chan, M. Yamada, and H. Inaba, "Micrometer-resolution, optical imaging of objects through highly scattering media using a heterodyne detector array," *Electron. Lett.* **30**(21), 1753–1754 (1994).
43. B. Devaraj, M. Usa, K. P. Chan, T. Akatsuka, and H. Inaba, "Recent advances in coherent detection imaging (CDI) in biomedicine: laser tomography of human tissues in vivo and in vitro," *IEEE J. Sel. Top. Quantum Electron.* **2**(4), 1008–1016 (1996).
44. K. P. Chan, K. Satori, and H. Inaba, "Laser imaging through scattering media by enhanced heterodyne detection and speckle averaging using 2D detector array," *Electron. Lett.* **34**(11), 1101–1103 (1998).
45. G. Jarry, E. Steimer, V. Damaschini, M. Epifanie, M. Jurczak, and R. Kaiser, "Coherence and polarization of light propagating through scattering media and biological tissues," *Appl. Opt.* **37**(31), 7357–7367 (1998).
46. K. F. Lee, F. Reil, S. Bali, A. Wax, and J. E. Thomas, "Heterodyne measurement of Wigner distributions for classical optical fields," *Opt. Lett.* **24**(11), 1370–1372 (1999).
47. Y. Watanabe, T. Yuasa, B. Devaraj, T. Akatsuka, and H. Inaba, "Transillumination computed tomography of high scattering media using laser linewidth broadening projections," *Opt. Commun.* **174**, 383–389 (2000).
48. Y. Sasaki, S. Tanosaki, J. Suzuki, T. Yuasa, H. Taniguchi, B. Devaraj, and T. Akatsuka, "Fundamental imaging properties of transillumination laser CT using optical fiber applicable to bio-medical sensing," *IEEE Sens. J.* **3**(5), 658–667 (2003).
49. M. Strojnik and G. Paez, "Radiometry," in *Handbook of Optical Engineering*, D. Malacara and B. Thompson, eds., pp. 649–699, Marcel Dekker, New York (2001).
50. P. Vacas-Jacques, M. Strojnik, and G. Paez, "Optimal source bandwidth for pass-through photon-based trans-illumination interferometry," *Proc. SPIE* **6847**, 68472S (2008).
51. J. Schmitt, "Optical coherence tomography (OCT): a review," *IEEE J. Sel. Top. Quantum Electron.* **5**(4), 1205–1215 (1999).
52. L. Mandel, "Fluctuations of photon beams: the distribution of the photo-electrons," *Proc. Phys. Soc.* **74**, 233–243 (1959).
53. P. Vacas-Jacques, M. Strojnik, and G. Paez, "Monte-Carlo simulation of photon trans-illumination time of flight," *Proc. SPIE* **6631**, 663114 (2007).
54. Laser Institute of America, *ANSI Z136.1-2007: American National Standard for Safe Use of Lasers*, pp. 77, American National Standard, Orlando, FL (2007).
55. S. Flock, B. Wilson, and M. Patterson, "Total attenuation coefficients and scattering phase functions of tissues and phantom materials at 633 nm," *Med. Phys.* **14**(5), 835–841 (1987).
56. B. Pogue and M. Patterson, "Review of tissue simulating phantoms for optical spectroscopy, imaging and dosimetry," *J. Biomed. Opt.* **11**(4), 041102 (2006).
57. H. van Staveren, C. Moes, J. Marle, S. Prahl, and M. van Gemert, "Light scattering in Intralipid-10% in the wavelength range of 400-1100 nm," *Appl. Opt.* **30**(31), 4507–4514 (1991).
58. G. Jarry, L. Poupinet, J. Watson, and T. Lepine, "Extinction measurements in diffusing mammalian tissue with heterodyne detection and a titanium:sapphire laser," *Appl. Opt.* **34**(12), 2045–2054 (1995).
59. R. Jones and D. Fried, "Attenuation of 1310 and 1550-nm laser light through dental enamel," *Proc. SPIE* **4610**, 187–190 (2002).
60. R. Jones, G. Huynh, G. Jones, and D. Fried, "Near-infrared transillumination at 1310-nm for the imaging of early dental decay," *Opt. Express* **11**(18), 2259–2265 (2003).
61. R Development Core Team, *R: A Language and Environment for Statistical Computing*, R Foundation for Statistical Computing, Vienna (2008).
62. J. Lemon, B. Bolker, S. Oom, E. Klein, B. Rowlingson, H. Wickham, A. Tyagi, O. Eterradossi, and G. Grothendieck, *Plotrix: Various Plotting Functions*, R package version 2.2, ggrothendieck@gmail.com (2008).